Materials & Design 128 (2017) 166–175

Contents lists available at ScienceDirect

Materials & Design

journal homepage: www.elsevier.com/locate/matdes

Dissimilar laser welding of superelastic NiTi and CuAlMn shape memory alloys

J.P. Oliveira[a,b,c,*], Z. Zeng[d], C. Andrei[e], F.M. Braz Fernandes[c], R.M. Miranda[f], Antonio J. Ramirez[c], T. Omori[g], N. Zhou[b]

[a] Department of Materials Science and Engineering, The Ohio State University, 1248 Arthur E. Adams Drive, Columbus, OH 43221, USA
[b] Centre for Advanced Materials Joining, University of Waterloo, Canada
[c] CENIMAT/i3N, Faculdade de Ciências e Tecnologia, Universidade Nova de Lisboa, Portugal
[d] School of Mechanical, Electronic, and Industrial Engineering, University of Electronic Science and Technology of China, China
[e] Canadian Center for Electron Microscopy, Brockhouse Institute for Materials Research, McMaster University, Canada
[f] UNIDEMI, Faculdade de Ciências e Tecnologia, Universidade Nova de Lisboa, Portugal
[g] Department of Materials Science, Graduate School of Engineering, Tohoku University, Japan

ARTICLE INFO

Keywords:
Shape memory alloys
Dissimilar welding
Laser welding
Transmission electron microscopy
Superelasticity

ABSTRACT

Dissimilar joining of advanced engineering alloys is fundamental for the development of new applications. However, joining two distinct materials poses difficulties owing to the several metallurgical and thermo-physical problems that can arise. This paper describes the work performed on dissimilar laser welding of NiTi and CuAlMn shape memory alloys, superelastic at room temperature. Detailed microstructural characterization was performed. The complex microstructure of the dissimilar joint is explained based on the characteristics of laser welding, namely material and heat flow, high cooling rates and thermal gradients within the fusion zone. Cycling tensile testing revealed that the joints preserved the superelastic behaviour despite the unfavourable microstructure of the fusion zone which translates into an irrecoverable strain of 2% when cycled at 5% strain. These results may open the possibilities for new applications based on this dissimilar combination which can combine superelasticity and higher thermal and electrical conductivity (with the latter two characteristics arising for the CuAlMn shape memory alloy).

GRAPHICAL ABSTRACT

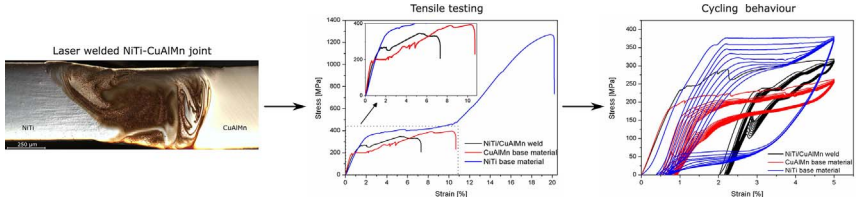

1. Introduction

Shape memory alloys are a class of functional materials that exhibit two very distinct properties: the shape memory effect and superelasticity. These properties occur due to the reversible martensitic transformation between a high temperature phase (austenite) and a low temperature one (martensite). Owing to these characteristics, shape memory alloys have found several relevant applications for several industries including biomedical, aerospace and automotive [1–5].

Among the different classes of shape memory alloys, NiTi is the most used one [6]. However, owing to the high production costs of NiTi, which are due the raw materials used but also to the need for a very precise composition and protective atmosphere during its manufacturing, other alloys have emerged as possible substitutes. Cu-based shape memory

* Corresponding author at: Department of Materials Science and Engineering, The Ohio State University, 1248 Arthur E. Adams Drive, Columbus, OH 43221, USA.
E-mail addresses: desousaoliveira.1@osu.edu, jp.oliveira@campus.fct.unl.pt (J.P. Oliveira).

http://dx.doi.org/10.1016/j.matdes.2017.05.011
Received 10 March 2017; Received in revised form 30 March 2017; Accepted 5 May 2017
Available online 08 May 2017

alloys are significantly less expensive than NiTi and have higher electrical and thermal conductivities, which make them prone to be used in electrical actuated systems for example. Although there are various Cu-based alloys (Cu-Al-Ni [7] or Cu-Al-Be [8]), Cu-Al-Mn shape memory alloys have emerged as one of the most interesting ones due to the possibility to significantly change their mechanical response by modifying its grain size [9]. Both NiTi [10,11] and CuAlMn [12,13] shape memory alloys found applications in the biomedical industry owing to their biocompatibility properties.

In order to take advantage of the properties exhibited by two distinct materials, joining methods are often used. Welding of shape memory alloys is mostly devoted to NiTi in similar combinations [14–21], although recent works have focused on the weldability of Cu-based shape memory alloys [22–24]. Despite the wide range of welding techniques used for shape memory alloys (resistance welding [25], gas tungsten arc welding [26,27], brazing [28,29], explosion [30] and electron beam welding [31] are some examples) laser welding is by far the most used [32–38]. This is related to the characteristics of the technique which allows for a very narrow thermally affected zones which can be detrimental for the functional properties of these materials [39].

Dissimilar joining can pose significant problems due to different thermo-physical properties of the base materials [40,41]. The weldability of the dissimilar couple will be determined by their atomic diameter, crystal structure and compositional solubility in both liquid and solid state [42]. If the materials to be joined have significantly different coefficients of thermal expansion the joint may fail during solidification due to residual stresses. Such residual stresses can, for example, dramatically change the fatigue life and dimensional stability of the structure [43]. Although segregation often occurs in fusion-based processes, the high cooling rates associated with laser welding, in the order of 10^4–10^5 K/s [44], decrease this phenomenon. In opposition, the higher thermal gradients experienced during welding may promote high resultant stresses which can be detrimental to the joint performance.

Dissimilar joining involving NiTi was already reported successfully to occur with several materials. Gugel et al. [45,46], reported joining of NiTi to steel using a laser with steel. Of special relevance of these works is that fact that the dissimilar joint presented superelastic behaviour when cycled up to 2.5% strain. Laser welding was also used to join NiTi to stainless steel [47–49]. In-situ mechanical analysis of the joint was performed in [47] to observe the fracture behaviour during mechanical solicitation of the joint. In a follow-up work [48], three dimensional chemical analysis was performed to further understand the metallurgical reactions that occurred in the fusion zone of the welded. Finally, Hahnlen et al., [49] successfully joined NiTi and stainless tubes and were able to decrease the extension of the heat affected zone on the NiTi side by careful selection of the welding procedure.

Recently, NiTi and Ti6Al4V were also joined, despite the mechanical properties of the joint were affected by the presence of brittle intermetallics [50]. The use of a Nb interlayer in between the two base materials was able to suppress mixing of the two base material and therefore avoided the formation of undesired intermetallic compounds [51]. Joining of NiTi to aluminium was also achieved through ultrasonic techniques [52,53] and hybrid friction stir welding [54]. To date there are no reports on dissimilar joining attempts involving Cu-based shape memory alloys.

In this work laser welding was used to join NiTi and CuAlMn shape memory alloys. Defect-free joints were obtained and superelasticity was preserved after welding.

Table 1
Melting temperature, T_m, and thermal conductivity of the two base materials used.

Material	T_m [°C]	Thermal conductivity [W/K·m]
NiTi	1315	18
CuAlMn	948	21

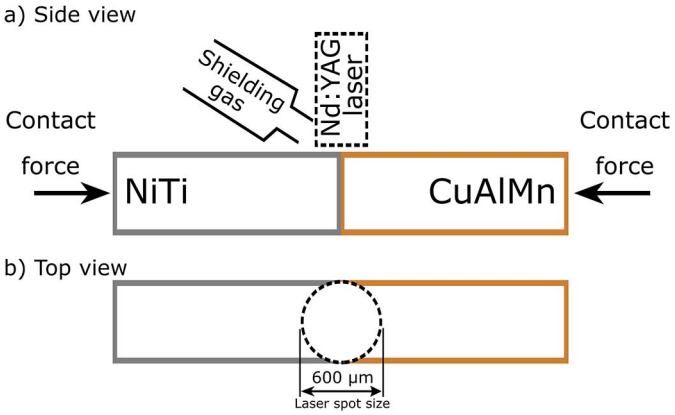

Fig. 1. Experimental set-up used for laser welding NiTi and CuAlMn shape memory alloys (not to scale): a) side view; b) top view.

2. Experimental procedure

2.1. Materials

In this work two different shape memory alloys were used: Cu17Al11Mn (at.%) and 50.8NiTi (at.%). The CuAlMn alloy was prepared by induction melting in Argon inert atmosphere. The as-casted ingot was hot forged and subsequently cold drawn to obtain 0.5 mm in diameter wires. The wires were then solution heat treated at 900 °C followed by quenching in water. To stabilize the transformation temperatures of the wires further aging at 200 °C was performed. The 0.5 mm in diameter NiTi wires were supplied by McMaster-Carr. Both alloys used in this work were austenitic at room temperature and therefore superelastic. The melting temperature, T_m, and thermal conductivity of the two base materials are presented in Table 1.

Prior to welding, the surface oxide of the wires was carefully removed using 1200 fine SiC paper, leading to a final wire diameter of 0.490 ± 0.005 mm. Then, the wires were cleaned using acetone and ethanol to remove any possible impurities in their surface.

2.2. Laser welding

Laser welding was performed using a Miyachi Unitek LW50A pulsed Nd:YAG laser system, which has a wavelength of 1.064 µm. A top-hat spatial profile with a spot size of 600 µm was used. The pulse profile had a duration of 6 ms, which included 1 ms up and downslope. Laser butt welds of NiTi to CuAlMn were performed using a peak power of 1.2 kW and the laser was positioned on the interface between the two base materials. Ar was used as shielding gas with a flow rate of 0.57 m^3/h and it was opened 10 s prior to welding in order to create a protective atmosphere to avoid oxidation of the fusion zone and its surroundings. In order to optimize joint fit-up, the joining surfaces were put in intimate contact through a contact force applied on the base materials. The experimental set-up used is depicted in Fig. 1.

2.3. Microstructural characterization

Optical microscopy was performed in the cross section of the joint. Macro and micrographs were taken after etching the cross section of the joint using Kroll's etching reagent for 15 s. As a result of the chemical heterogeneity throughout the welded region preferential etching of the microstructure occurred. Nonetheless, it was still possible to observe the microstructural details resulting from the welding procedure. Scanning electron microscopy (SEM) was performed using a FEI/Philips Sirion Field Emission SEM.

Transmission electron microscopy (TEM) was performed to analyse the joint interfaces between the fusion zone and each one of the base materials. Focused ion beam (FIB), using a Zeiss NVision 40, was used to prepare 10 × 10 µm specimens through the lift-out technique [55]. TEM

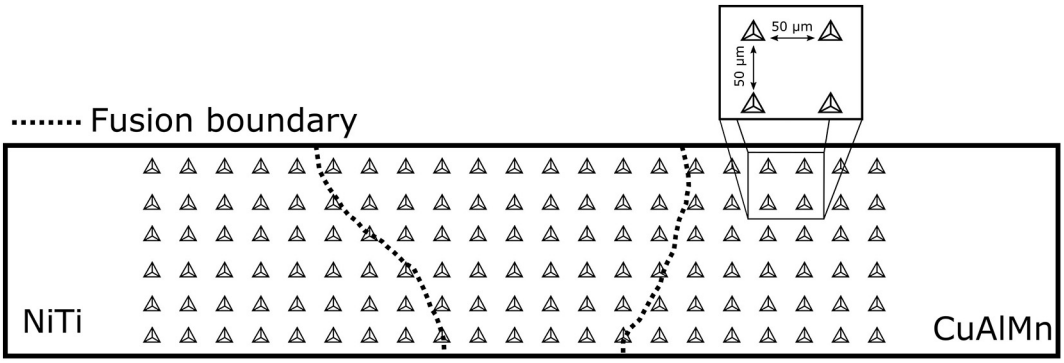

Fig. 2. Schematic representation of the hardness measurements.

experiments were performed using a JEOL 2010F TEM/STEM operated at 200 kV equipped with an Oxford Inca energy dispersive X-ray (EDS) system. Scanning TEM (STEM) images were obtained using a 1 nm probe.

2.4. Mechanical testing

A microhardness map was performed on the cross section of the NiTi/CuAlMn joint, using a Vickers hardness mapping device LECO LM100AT with 50 g load and 50 μm step size. This map covered a region of 1550 × 350 μm from base material to base material, as schematically depicted in Fig. 2.

Mechanical analysis of the base materials and welded joints consisted on tensile tests to fracture and 10 load/unload cycles up to 5% strain to analyse the superelastic behaviour. This characterization was performed using an Instron model 5548 micro-tensile tester. The displacement rate was set at 0.5 mm/min and a measurement accuracy was of ± 0.5 μm. Three samples for each condition (base materials and welded joints) were tested. The gauge length of the specimens was of 20 mm. The fracture surfaces were analysed by scanning electron microscopy using a Zeiss Leo 1550 Field Emission SEM equipped with an INCA energy 350 EDS microanalysis system.

3. Results and discussion

3.1. Microstructural characterization

A defect-free joint, with no cracking or pores, was obtained. Fig. 3 depicts the macrograph of the cross section of the NiTi/CuAlMn joint. In fusion welding of dissimilar materials the mass and heat transfer processes have a significant impact in the fluid dynamics of the joint. Heat and mass losses due to preferential vaporization of elements can occur and change the dynamics within the weld pool. The most important driving force for fluid flow during fusion welding is the Marangoni effect. This effect occurs due to the different densities in the phases formed in the weld pool, temperature gradient, as well as to the gradient of surface-tension in the weld pool and dictates the fluid flow pattern obtained after welding. As a result of this, a complex flow pattern observed in Fig. 3. Since the gradient of surface-tension is temperature dependent, a large difference in the fluid flow occurs throughout the fusion zone.

Owing to the complex microstructure observed throughout the fusion zone of the dissimilar joint between NiTi and CuAlMn the microstructural characterization of each zone is analysed separately. This characterization was performed by optical, scanning and transmission electron microscopies. Before analysing in detail the regions A to D of Fig. 3, attention will be given to the macrosegregation phenomena observed in regions marked with arrows in the macrograph (Fig. 3).

3.1.1. Macrosegregation in the fusion zone

As mentioned before, the arrows presented in Fig. 3 indicate regions where macrosegregation in the weld metal is observed. The black arrow points to a region which has a composition close to that of the NiTi base material, while the blue arrows indicate the regions within the fusion zone that have similar composition as the CuAlMn base material. These compositional measurements were performed by SEM-EDS and are of 49.5 at.% Ni, 49.3 at.% Ti and 1.2 at.% Cu for the macrosegregation region with NiTi-like composition and 71.2 at.% Cu, 14.9 at.% Al, 10.7 at.% Mn, 2.1 at.% Ni and 1.1 at.% Ti for the CuAlMn-like region. The higher loss of aluminium compared to the original base material may be related to the lower evaporation temperature of this element.

A thin foil for TEM analysis from the region corresponding to the macrosegregation of NiTi (black arrow in Fig. 3) was prepared using focused ion beam. Fig. 4 depicts a bright-field STEM image and corresponding EDS map from the macrosegregation region previously identified as having a NiTi-like base material composition. A fine grain structure, with grain size ranging between 1 and 2 μm is observed. EDS point analysis on this region confirmed the composition measured by SEM-EDS analysis. In fact, the compositional sum of Cu, Al Mn is less than 4 at.%, with Cu having nearly 2 at.%. Moreover, from the EDS maps it is clear that Cu was preferentially segregated towards the grain boundaries of these regions. Mn also shows some evidence of preferential segregation towards the grain boundaries, while Al is mainly observed inside the grains. Since complete mixing did not occur in this particular region Cu,

Fig. 3. Macrograph of the NiTi/CuAlMn dissimilar laser joint. Regions A to D are analysed separately. The black and blues arrows indicate regions where macrosegregation occurred: black for NiTi and blue for CuAlMn. (For interpretation of the references to colour in this figure legend, the reader is referred to the web version of this article.)

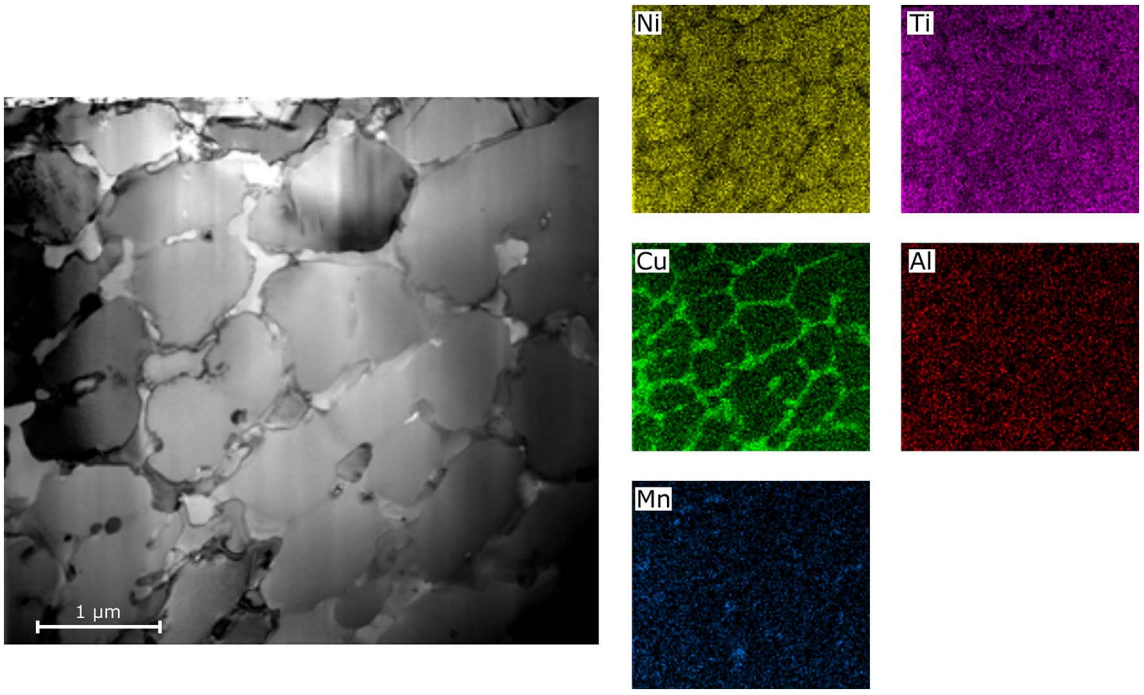

Fig. 4. Bright-field STEM image on the NiTi macrosegregation region and corresponding EDS maps.

Al and Mn have diffused into the unmixed zone with a composition similar to that of the original NiTi base material.

Macrosegregation can occur due to the compositional difference between the materials to be welded. Several authors have reported macrosegregation features by referring to them as base-metal like "beaches", "peninsulas" or "islands". In this work, these islands of unmixed base material are seen to occur in both the NiTi side of the fusion zone as well as in the CuAlMn side. Moreover, a region near the NiTi base material which has the same composition of the CuAlMn alloy is also observed (blue arrow on the left of Fig. 3). This particular region is analysed in subsection "Region C – macrosegregation with dendrite fragmentation".

Soysal et al. [56] discussed the mechanisms for macrosegregation in a dissimilar joint of Cu and steel considering the simple Cu-Fe phase diagram. They illustrated how these regions can be formed in dissimilar welding of Cu to Fe, basing their reasoning on the analysis of the Cu-Fe phase diagram. The mechanisms responsible for such features are related to the liquidus temperature of the base materials and of the weld metal. When similar welding is performed, the liquidus temperature of the base material, T_{LBM}, is equal to that of the weld metal, T_{LWM}. However, in dissimilar welding the composition of the fusion zone is distinct from the two base materials, thus its liquidus temperature (T_{LWM}) will be higher or lower than the one of base materials (T_{LBM1} and T_{LBM2}).

The macrosegregation features will be affected by the relative liquidus temperature of the weld metal and of the base materials. If the liquidus temperature of the weld pool is lower than the liquidus temperature of the base material a peninsula or island of base material composition can form. On the other hand, if the liquidus temperature of the weld metal is higher than that of the base material an irregular-shaped beach with the composition of the base material can be formed. Since the macrograph presented in Fig. 3 has only islands of both base materials, one can infer that the liquidus temperature of the weld pool for the NiTi-CuAlMn weld was lower than the liquidus temperature of both base materials. This might have occurred due to the eutectic reactions in the NiTi-Cu system.

The reason for the formation and movement of these islands of unmixed base material can be explained as follows: due to the reduced fluid flow in the proximity of the molten pool boundary a layer of unmixed base material in the liquid state can form. This layer has the same or very similar composition to that of the base material from which it was originated. Since the bulk of the weld pool has a composition different from both base materials, its liquidus temperature is different. Then, due to convection, this unmixed layer can move towards the weld pool. However, due to the decrease in the liquidus temperature in the weld pool, the unmixed region will be a region where the temperature is below its liquidus temperature. As a result, quick solidification of this unmixed region occurs and without mixing with the surrounding liquid.

Additionally, Soysal et al. [56] used gas-tungsten arc welding as with this technique the fluid flow in the fusion zone is easier to analyse, more stable and better understood. In opposition, for laser welding there are several factors that cause the fluid flow to be more complex. As a result of this highly complex fluid flow typical of laser welding, the chemical homogeneity of the weld metal may only occur locally. As such, the formation of islands of base metal composition previously identified may have occurred due to the decrease of the liquidus temperature of the weld metal near both base materials, in relation with the eutectic reactions of the NiTi-Cu system. This situation allowed for the unmixed layers of base

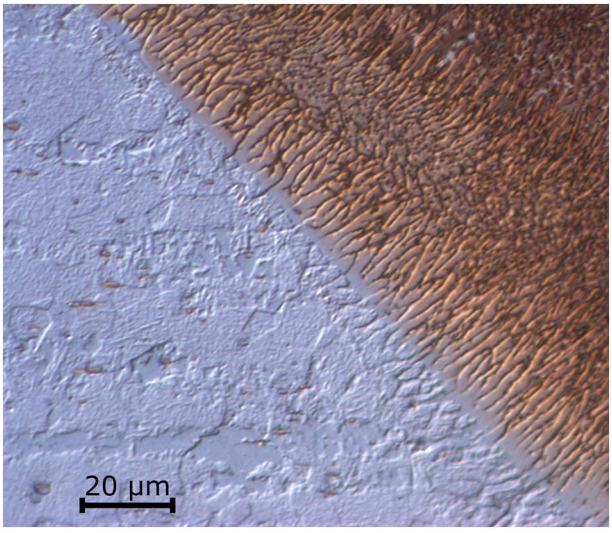

Fig. 5. NiTi base material and fusion boundary interface. This figure corresponds to region A of Fig. 3.

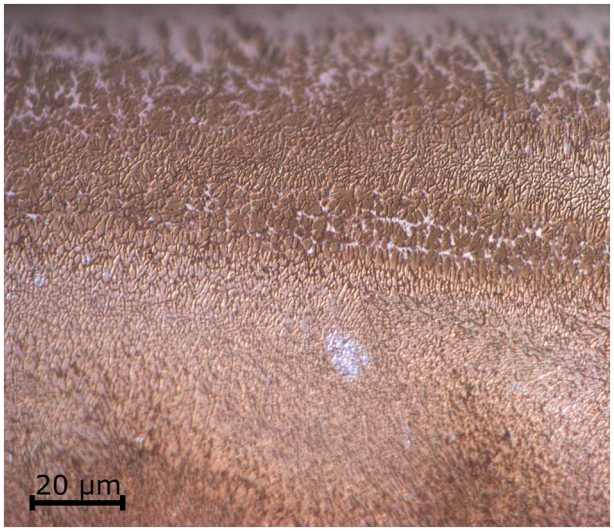

Fig. 6. Evidence of columnar to equiaxed dendrite growth in the fusion zone.

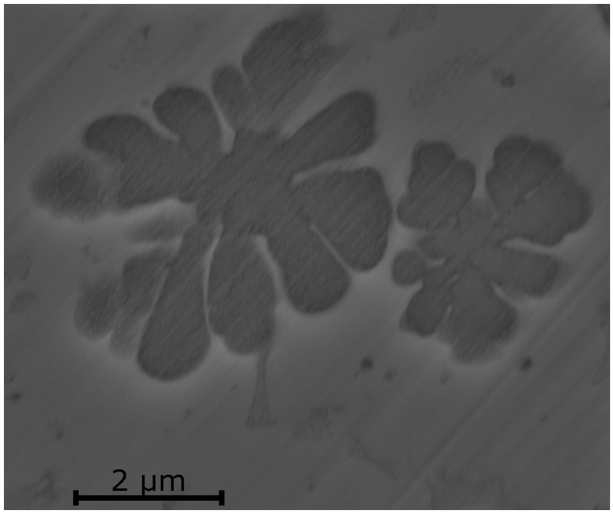

Fig. 7. SEM image of equiaxed dendrites.

material to move towards these low temperature regions and quickly freeze.

3.1.2. Region A – NiTi base material/fusion zone interface

Fig. 5 depicts a micrograph of the fusion boundary on the NiTi side. In welding, solidification of the weld pool is nucleated by the solid crystals located at the solid-liquid interface. This form of crystal growth is known as epitaxial growth. There are five distinct types of growth modes that can occur (alone or in combination) in fusion welding: planar, cellular, cellular dendritic, columnar dendritic and equiaxed dendritic. The temperature gradient, G, solidification rate, R, and composition are found to greatly influence the solidification modes observed in fusion welding. Usually, a planar interface is not stable and easily breaks down into a cellular or cellular dendritic growth front. Increasing the solidification rate causes the solidification mode to change from cellular to cellular dendritic and then to columnar dendritic. Owing to the large supercooling required, equiaxed dendritic growth is not normally observed in fusion welding. All but equiaxed dendritic growth structures were observed in the micrograph presented in Fig. 5. However, further into the fusion zone, evidence of equiaxed dendrites is observed in both optical and scanning electron microscopy (Fig. 6). This equiaxed dendritic structure is discussed in the following subsection.

Formation of columnar or equiaxed dendrites in the fusion zone can be explained based on the thermal gradient and growth rate. In fusion welding the degree of undercooling is known to be inversely proportional to the ratio between thermal gradient and growth rate (G/R). Within the weld pool, the thermal gradient is more severe near the fusion boundary, that is, near the initial base material, than in the weld centreline. In the presence of severe thermal gradients, as those usually found near the fusion boundary, columnar dendritic growth is favoured and it occurs in the opposite direction of the heat flow extraction; that is, these columnar dendrites grow towards the weld centreline, but not necessarily perpendicular to the fusion boundary, since this bends locally, depending on the weld travel speed. From the fusion boundary towards the weld centreline the thermal gradient decreases. Combining this decrease of the thermal gradient and the fast cooling rate typical of laser welding [40], significant undercooling occurs, favouring the formation of equiaxed dendrites.

3.1.3. Region B – columnar to equiaxed transition

Further into the fusion zone, it is clear a columnar to equiaxed transition growth (Fig. 6). When these equiaxed dendrites start to nucleate and develop, due to the high undercooling experienced, they block off the columnar dendrites. Generally speaking, an equiaxed grain structure tends to be more desirable than a columnar one [57]. This is related to the fact that with an equiaxed structure there is less alloying segregation which allows one to obtain a more isotropic microstructure, with more homogenous composition.

3.1.4. Region C – macrosegregation with dendrite fragmentation

Although the columnar to equiaxed dendritic growth is observed in the majority of the fusion zone there are regions where equiaxed dendrites are found alone. Such dendrites are found, for example, in region C of Fig. 3.

Fig. 7 depicts a SEM image of those equiaxed dendrites found in region C. EDS measurements performed within the dendrite revealed that these structures are mainly Cu-rich ($\approx$ 46 at.%). Near the same amount of both Ni and Ti ($\approx$ 16 at.% each), and Al and Mn having approximately 16 and 6 at.%, respectively, were found. In the interdendritic space and surrounding matrix, the composition is completely different, being similar to the CuAlMn base material, with trace amounts of Ni and Ti (less than 2 at.%).

Nucleation within the weld pool can occur through heterogeneous nucleation (if there are particles in the weld pool that can act as heterogeneous nuclei), grain detachment (if partially melted grains go into the weld pool and act as nuclei) or dendrite fragmentation (if the weld pool convection promotes fragmentation of the dendrite tips and these act also as new nuclei). From these three hypotheses and analysing the macrograph of the joint presented in Fig. 8, it is apparent that the equiaxed dendrites where formed due to dendrite fragmentation.

Since intense convection is typical of laser welding [42], it is possible that it caused dendrite fragmentation. By analysing the macrograph of the joint, it can be inferred that these dendrites follow the fluid flow in that region of the weld, which was created by convection but also by the

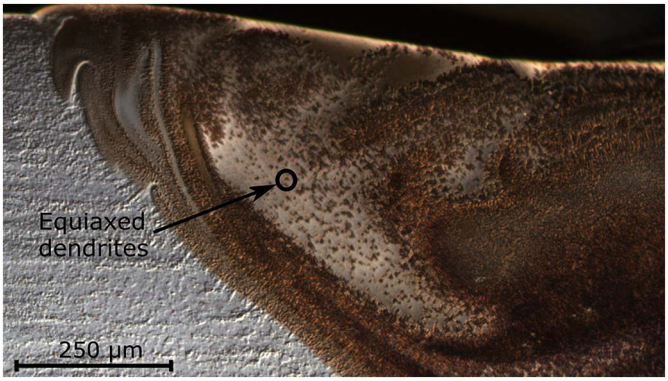

Fig. 8. Close-up of the region where dendrite fragmentation into a CuAlMn base material-like composition region occurred. The circle represents a region analysed in Fig. 7 showing the equiaxed dendrites.

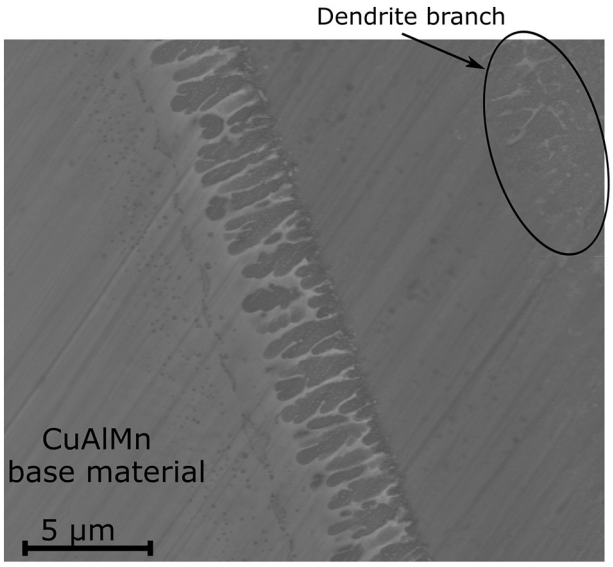

Fig. 9. Fusion boundary on the CuAlMn side.

different local densities in the fusion zone. It should be noticed that the equiaxed dendrites existing in this region are not homogenously distributed in the CuAlMn base material-like composition region. Such feature should be related to the fact that this region experienced quick freezing thus preventing dendrite tips to move further into the liquid and growth.

This region, where dendrite fragmentation give rise to equiaxed dendrites, is also of special interest. EDS analysis revealed a composition similar to that of the original CuAlMn base material with Ni and Ti contents being below 2 at.%. This macrosegregation feature, similar to that described in the subsection "Macrosegregation in the fusion zone" should only have occurred near the CuAlMn base material. However, since the liquidus temperature of CuAlMn is significantly lower than that of NiTi (948 °C vs 1315 °C, respectively) melting of CuAlMn occurs first which allows for unmixed regions to travel into the bulk weld metal due to convection. In this case the unmixed region travelled almost towards the NiTi fusion boundary, but part of this unmixed liquid incorporated dendrite tip which then has grown in a equiaxed-like morphology.

3.1.5. Region D – CuAlMn base material/fusion zone interface

The microstructure of region D, corresponding to the fusion boundary of the CuAlMn side, is not easily observed by optical microscopy, hence scanning electron microscopy was performed to analyse it. Fig. 9 depicts a SEM image of the CuAlMn fusion boundary. Similarly, to what was observed on the NiTi fusion boundary, planar, cellular and columnar dendritic grain growth are observed. However, in the CuAlMn fusion boundary these grain structures are significantly smaller than in the opposite fusion boundary.

From Fig. 9 it can be also observed that the columnar growth is abruptly stopped and no evident grain structure is noticed. EDS analysis of the region in front of the columnar dendrites revealed that this region had and equiatomic amount of Ni and Ti (≈ 48 at.%), with trace amounts of Cu (≈ 4 at.%). This region has an extension of roughly 5 to 10 μm and there a dendrite branch can be observed (top right side of Fig. 9).

Analysing the region just ahead of the dendrite observed in Fig. 9, reveals more isolated dendrites branches (Fig. 10). Again, EDS analysis reveals that the dendrites are mainly Cu-rich (≈ 59 at.%), with the same similar amount of Ni and Ti (≈ 14 at.% each) and with trace amounts of Mn and Al (8 and 5 at.%, respectively). The surrounding matrix has the same composition determined in the region ahead of the columnar dendrites at the CuAlMn fusion boundary, that is, Ni and Ti with nearly 48 at.% each, and trace amounts of Cu (≈ 2 at.%). From this it can be concluded that island of NiTi-like compositions formed on the NiTi fusion boundary were also able to travel towards the opposite fusion boundary.

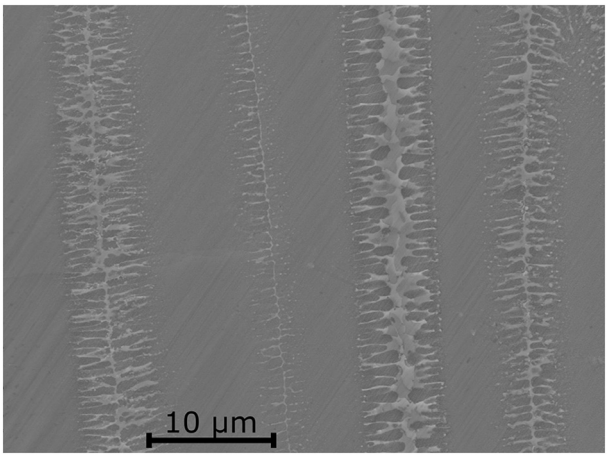

Fig. 10. Isolated columnar dendrite branches near the CuAlMn interface.

However, their size is significantly smaller than the islands of CuAlMn-like composition presented before.

Of special interest is also the morphology of the dendrites shown in Fig. 10. Dendrite size is related to the cooling rate experienced during solidification: higher cooling rates give origin to smaller dendrites. Significant differences in size are observed in the dendrites shown in Fig. 10, so they have experienced different cooling rates. It is possible that the complex fluid flow pattern observed for this dissimilar combination may have influenced such dendritic growth. Compared with the dendrites observed on the NiTi side, it is observed that those formed in the CuAlMn side have a smaller size. This is related with the cooling conditions experienced during welding. Since, the thermal conductivity of CuAlMn is higher than that of NiTi (21 vs 18 W/K·m, respectively), higher cooling rates are experienced near the CuAlMn side. As a result, a very fine grain structure, with dendrite arm spacing ranging between 0.45 and 0.85 μm, was developed.

In between the arms of the dendritic structure just ahead of the CuAlMn fusion boundary, evidence of secondary particles was noticed although these were not clearly resolved using SEM. As such, a thin foil containing this region was prepared using focused ion beam for TEM analysis.

Fig. 11 depicts the TEM image of the second-phase particles encountered in the interdendritic space of the CuAlMn fusion boundary. EDS analysis performed on this region of the TEM specimen revealed a

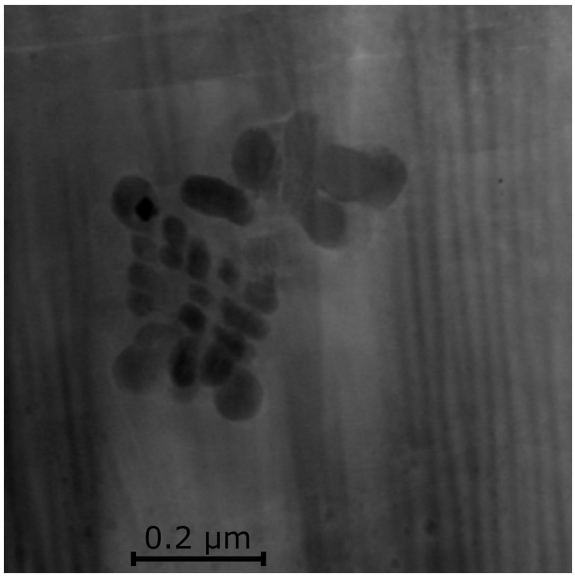

Fig. 11. STEM image of second-phase particles in the interdendritic space of the CuAlMn fusion boundary.

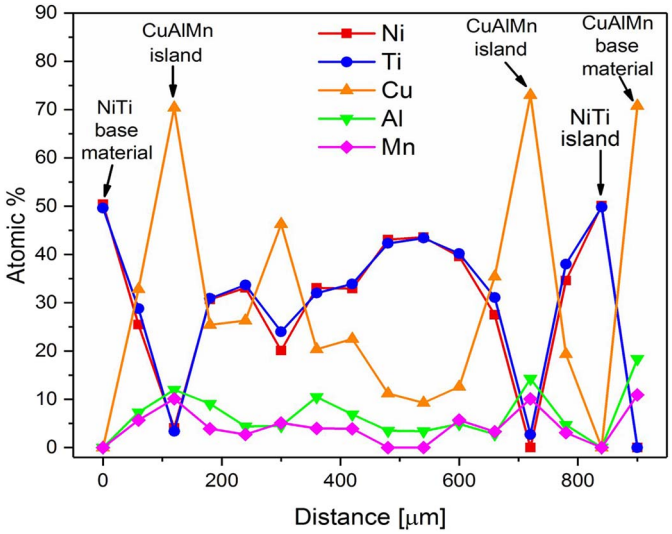

Fig. 12. SEM-EDS point analysis performed in the welded joint. CuAlMn islands were identified.

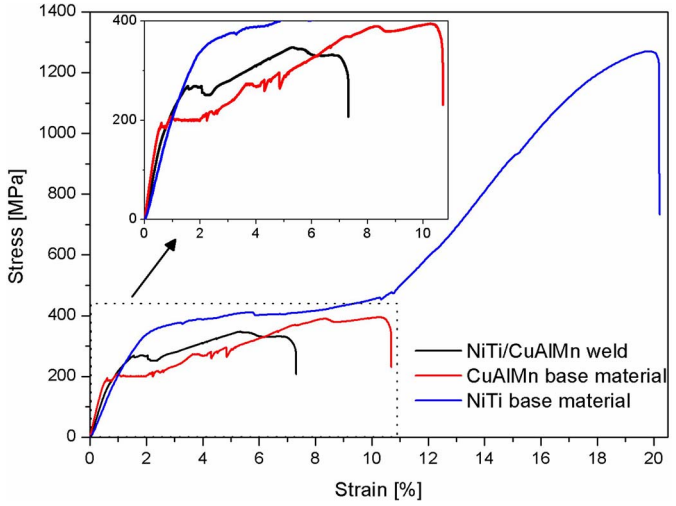

Fig. 14. Stress-strain curves of the NiTi and CuAlMn base material and of their dissimilar joint. The insert depicts a more detailed view of the stress-strain curves of both the CuAlMn base material and of the welded joint.

composition of 41.6Cu-21.9Ti-20.2Al-13.7Ni-2.6Mn (at.%), that is, a complex mixture of all the elements that compose the two base materials. No reports of precipitates with similar compositions where found in the literature, although Cu-Al-Ni-Ti-Mn shape memory alloys have been investigated previously. For such alloy system Ti and Mn are present in minor quantities to promote grain refinement (Ti) and to improve ductility (Mn) [6].

3.2. Compositional changes along the fusion zone

SEM-EDS point analysis was performed approximately at mid-height of the welded joint, starting in the NiTi base material, crossing the fusion zone and finishing on the CuAlMn base material. Despite SEM-EDS is a semi-quantitative technique, it is still possible to observe the trend along the fusion zone, as presented in Fig. 12. It can be observed that the atomic percentage of Ni and Ti are always similar through the fusion zone. Additionally, two CuAlMn islands, as well as one NiTi island, are clearly identified near the base materials, which is in good agreement with the previous microstructural characterization. It is possible that preferential evaporation of lighter elements, such as Al, has occurred during welding. For example, in laser welded CuZnAl shape memory alloy, Zn loss has been reported [24].

3.3. Microhardness mapping

Fig. 13 depicts the microhardness map of the dissimilar NiTi/CuAlMn joint. A good agreement with the macrograph presented in Fig. 3 is evident. In particular, region C which was identified as an unmixed beach of CuAlMn-like composition presents a hardness close to the of the base material from which it was originated. Within the fusion zone the hardness is significantly higher than in the two base materials. This is related to the high amounts of Ni, Ti and Cu in the thoroughly mixed regions of the fusion zone. It is known that in $Ti_xNi_yCu_z$ (x, y, z in at.%) compounds when z is higher than 10 at.% and x ≈ y then the structure becomes harder and brittle [58].

3.4. Tensile behaviour

The stress-strain curves of both materials as well as of the dissimilar laser welded joint are presented in Fig. 14. It can be observed that the tensile strength and fracture of NiTi are significantly higher than the CuAlMn base material (1270 MPa vs 395 MPa for the tensile strength and 20.2% vs 10.7% for the fracture strain). Additionally, the superelastic plateau of NiTi starts at around 360 MPa while for the CuAlMn it required stress for the stress-induced transformation is of 190 MPa. As for the dissimilar laser weld of NiTi and CuAlMn it can be observed that the tensile strength and fracture strain as lower than any of the base material, with those values being of 350 MPa and 7.3%, respectively.

Fracture of the welded joints during tensile testing occurred in the fusion zone near the CuAlMn base material. It is known that the CuAlMn alloy used in this investigation does not present any heat affected zone after welding due to the previous heat treatments performed to optimize its superelastic properties [22]. Fracture surface of the CuAlMn side revealed ductile-like features as observed by the presence of microvoids (Fig. 15). Previously results on laser welding of CuAlMn revealed that fracture of the joints occurs in a ductile manner evidenced by the presence of microvoids [22].

The fracture surface on the NiTi side reveals three distinct regions (from A to C in Fig. 16). Regions A, which corresponds to a CuAlMn-like composition and reveals a ductile-like fracture surface, with a significant amount of dimples. In region B and C, the fracture mode changes to cleavage and quasi-cleavage, respectively.

The reason for having these three regions is related to the joint macrostructure. In the joint it was observed the presence of beaches with CuAlMn-like composition. It is known that for such compositions the material will fracture in a ductile manner. However, a significant portion of the fusion zone has higher hardness owing to the higher content of Ni, Ti and Cu in the fusion zone. During tensile testing the stress will be first accommodated by the soft material, which will be CuAlMn base material, followed by load transfer to NiTi. Eventually, the stress will be transferred to the fusion zone, where a harder and brittle structure is found. From that point on, little or no plastic deformation can be accommodated by

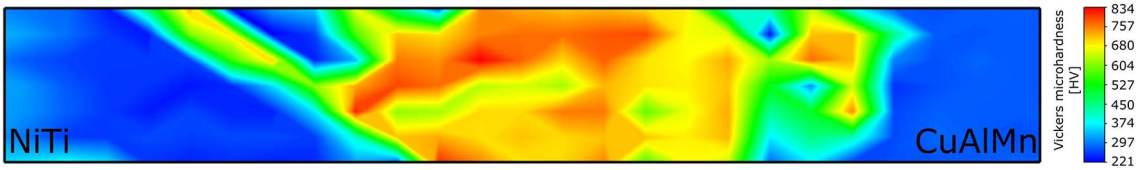

Fig. 13. Microhardness map of the NiTi/CuAlMn joint.

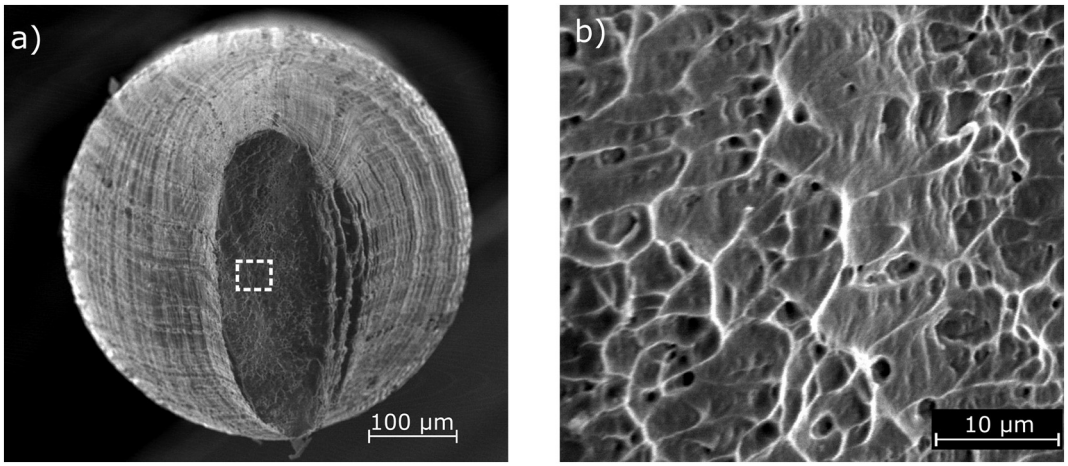

Fig. 15. Fracture surface of the CuAlMn side: a) overview; b) zoom of dashed square in a).

the fusion zone and fracture occurs with the characteristics evidenced in Figs. 15 and 16.

The superelastic behaviour of the dissimilar joint was analysed by performing a total of 10 load/unload cycles to 5% strain. Fig. 17 depicts the comparison between the NiTi/CuAlMn dissimilar joint and the two base materials. The superelastic plateau of the welded joints is clearly observed in the stress-strain curves depicted in Fig. 14 and it starts at around 200 MPa. This value lies between the required stress for the martensitic transformation of both base materials, and this was expected as the welded joints may be considered as composite composed of two shape memory alloys with distinct superelastic plateaus. Similar observations were observed when laser processing CuAlMn shape memory alloys, giving rise to a composite-like structure based on the microstructural modifications imposed [23].

The NiTi/CuAlMn joint presents a higher irrecoverable strain than that exhibited by the two base materials. This is related to a decrease in the superelastic properties of two base materials which compose the welded joint but also due to the unfavourable microstructure in the fusion zone.

It is known that during superelastic cycling of shape memory alloys martensite stabilization occurs, thus preventing complete superelastic recovery [59–61]. Such martensite stabilization may occur due to high

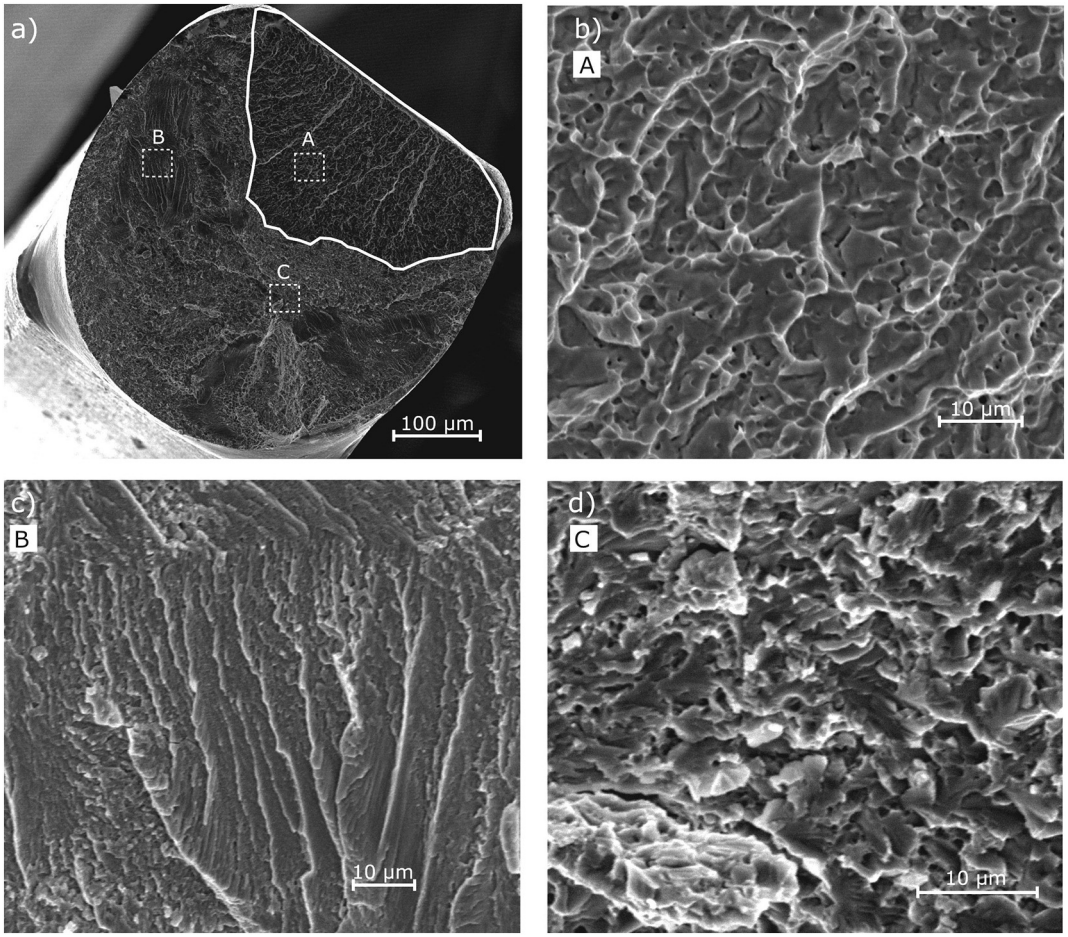

Fig. 16. Fracture surface on the NiTi side: a) overview; b) ductile-like fracture; c) cleavage fracture; d) quasi-cleavage fracture.

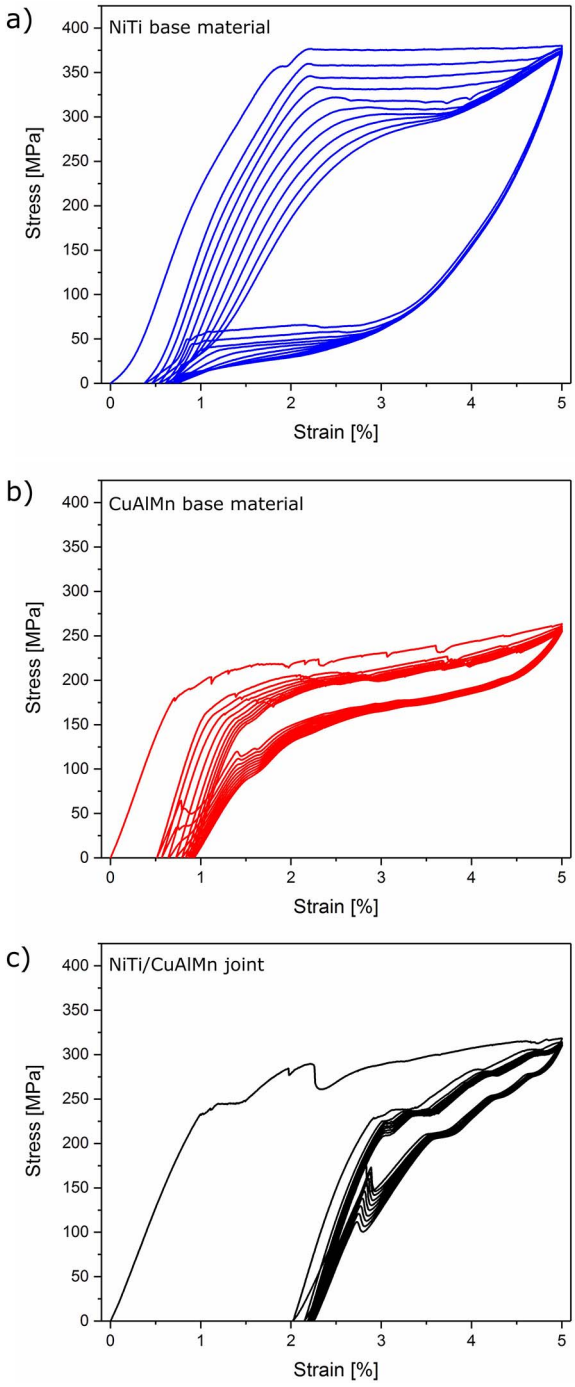

Fig. 17. Cycling behaviour of: a) NiTi base material; b) CuAlMn base material; c) NiTi/CuAlMn joint and comparison with the two base materials. The x and y scales were kept constant for a clearer comparison.

localized stresses at the interface of the martensitic transformation, promoting slip, even though the external applied stress is lower than the stress required for slip [62]. The microstructure of the fusion zone should be contributing to most of the irrecoverable strain presented by the joint: due to mixture of the two base materials, which promoted a compositional change relatively to the original compositions, it is not guaranteed that the majority of fusion zone exhibits any superelastic behaviour. As such, any deformation other than pure elastic will have an irreversible character.

Despite the higher irrecoverable strain after the first load/unload cycle (≈ 2%) compared to the base material, the superelasticity of the joint is still evident and a stable behaviour is observed. It can also be observed that with increasing number of load/unload cycles the external stress required for the stress induced transformation decreases. This is related to the increase in the internal stresses of the material, which require a lower external stress for inducing the martensitic transformation.

NiTi/CuAlMn joints exhibiting superelasticity may enable new possible applications where this functional property can be coupled with the high electrical conductivity of the CuAlMn base material.

4. Conclusions

Joining of NiTi to CuAlMn was performed by laser welding. This open new possibilities in terms of functional applications based on such dissimilar joints taking advantage of the functional properties of the two base materials coupled with the high thermal and electrical conductivity of CuAlMn. The major following conclusions can be drawn:

- Beaches of base material composition-like were formed in the fusion zone of the joint. This is related to the complex chemical composition of the fusion zone which had its liquidus temperature lower than those of the base materials.
- A complex microstructure was observed in the fusion zone: while columnar to equiaxed dendritic growth is observed in the majority of the joint, there are regions showing isolated equiaxed dendrites. These were formed by dendrite fragmentation and did not have time to grow significantly owing to quick freezing of the regions which involved them.
- The CuAlMn fusion boundary exhibits a finer grain structure than NiTi owing to the higher thermal conductivity of the former base material.
- The superelastic properties of the joint were preserved although an irrecoverable strain of 2% (for a maximum applied strain of 5%) was observed. This is mainly related to the unfavourable microstructure of the fusion zone.

References

[1] K. Kuribayashi, K. Tsuchiya, Z. You, D. Tomus, M. Umemoto, T. Ito, M. Sasaki, Self-deployable origami stent grafts as a biomedical application of Ni-rich TiNi shape memory alloy foil, Mater. Sci. Eng. A 419 (2006) 131–137, http://dx.doi.org/10.1016/j.msea.2005.12.016.
[2] D.J. Hartl, J.H. Mabe, O. Benafan, A. Coda, B. Conduit, R. Padan, B. Van Doren, Standardization of shape memory alloy test methods toward certification of aerospace applications, Smart Mater. Struct. 24 (2015) 82001, http://dx.doi.org/10.1088/0964-1726/24/8/082001.
[3] S. Shiva, I.A. Palani, S.K. Mishra, C.P. Paul, L.M. Kukreja, Investigations on the influence of composition in the development of Ni–Ti shape memory alloy using laser based additive manufacturing, Opt. Laser Technol. 69 (2015) 44–51, http://dx.doi.org/10.1016/j.optlastec.2014.12.014.
[4] K. Otsuka, X. Ren, Physical metallurgy of Ti-Ni-based shape memory alloys, Prog. Mater. Sci. 50 (2005) 511–678, http://dx.doi.org/10.1016/j.pmatsci.2004.10.001.
[5] O. Benafan, R.D. Noebe, S.A. Padula, D.W. Brown, S. Vogel, R. Vaidyanathan, Thermomechanical cycling of a NiTi shape memory alloy-macroscopic response and microstructural evolution, Int. J. Plast. 56 (2014) 99–118, http://dx.doi.org/10.1016/j.ijplas.2014.01.006.
[6] K. Otsuka, C.M. Wayman, Shape Memory Materials, Cambridge Press, Cambridge, 1998, http://dx.doi.org/10.1016/S1369-7021(10)70128-0.
[7] J. San Juan, M.L. Nó, C.A. Schuh, Superelastic cycling of Cu-Al-Ni shape memory alloy micropillars, Acta Mater. 60 (2012) 4093–4106, http://dx.doi.org/10.1016/j.actamat.2012.04.021.
[8] B. Kaouache, S. Berveiller, K. Inal, A. Eberhardt, E. Patoor, Stress analysis of martensitic transformation in Cu-Al-Be polycrystalline and single-crystalline shape memory alloy, Mater. Sci. Eng. A 378 (2004) 232–237, http://dx.doi.org/10.1016/j.msea.2003.10.348.
[9] Y. Sutou, T. Omori, K. Yamauchi, N. Ono, R. Kainuma, K. Ishida, Effect of grain size and texture on pseudoelasticity in Cu-Al-Mn-based shape memory wire, Acta Mater. 53 (2005) 4121–4133, http://dx.doi.org/10.1016/j.actamat.2005.05.013.
[10] L. Petrini, F. Migliavacca, Biomedical applications of shape memory alloys, J. Metall. 2011 (2011) 1–15, http://dx.doi.org/10.1155/2011/501483.
[11] M.H. Elahinia, M. Hashemi, M. Tabesh, S.B. Bhaduri, Manufacturing and processing of NiTi implants: a review, Prog. Mater. Sci. 57 (2012) 911–946, http://dx.doi.org/10.1016/j.pmatsci.2011.11.001.
[12] Y. Sutou, T. Omori, J.J. Wang, R. Kainuma, K. Ishida, Characteristics of Cu-Al-Mn-based shape memory alloys and their applications, Mater. Sci. Eng. A 378 (2004) 278–282, http://dx.doi.org/10.1016/j.msea.2003.12.048.
[13] Y. Sutou, T. Omori, A. Furukawa, Y. Takahashi, R. Kainuma, K. Yamauchi, S. Yamashita, K. Ishida, Development of medical guide wire of Cu-Al-Mn-base

superelastic alloy with functionally graded characteristics, J. Biomed. Mater. Res. B. Appl. Biomater. 69 (2004) 64–69, http://dx.doi.org/10.1002/jbm.b.10079.
[14] J.P. Oliveira, R.M. Miranda, F.M. Braz Fernandes, Welding and joining of NiTi shape memory alloys: a review, Prog. Mater. Sci. 88 (2017) 412–466, http://dx.doi.org/10.1016/j.pmatsci.2017.04.008.
[15] A. Tuissi, S. Besseghini, T. Ranucci, F. Squatrito, M. Pozzi, Effect of Nd-YAG laser welding on the functional properties of the Ni–49.6at.%Ti, Mater. Sci. Eng. A 273–275 (1999) 813–817, http://dx.doi.org/10.1016/S0921-5093(99)00422-0.
[16] J.P. Oliveira, R.M. Miranda, N. Schell, F.M. Braz Fernandes, N. Schell, F.M. Braz Fernandes, High strain and long duration cycling behavior of laser welded NiTi sheets, Int. J. Fatigue 83 (2016) 195–200, http://dx.doi.org/10.1016/j.ijfatigue.2015.10.013.
[17] J.P. Oliveira, F.M.B. Fernandes, N. Schell, R.M. Miranda, Shape memory effect of laser welded NiTi plates, Funct. Mater. Lett. 8 (2015) 1550069, http://dx.doi.org/10.1142/S1793604715500691.
[18] C.W. Chan, H.C. Man, F.T. Cheng, Fatigue behavior of laser-welded NiTi wires in small-strain cyclic bending, Mater. Sci. Eng. A 559 (2013) 407–415, http://dx.doi.org/10.1016/j.msea.2012.08.119.
[19] X.J. Yan, D.Z. Yang, Corrosion resistance of a laser spot-welded joint of NiTi wire in simulated human body fluids, J. Biomed. Mater. Res. Part A. 77 (2006) 97–102, http://dx.doi.org/10.1002/jbm.a.30378.
[20] A. Falvo, F.M. Furgiuele, C. Maletta, Laser welding of a NiTi alloy: mechanical and shape memory behaviour, Mater. Sci. Eng. A 412 (2005) 235–240, http://dx.doi.org/10.1016/j.msea.2005.08.209.
[21] C. Maletta, A. Falvo, F. Furgiuele, G. Barbieri, M. Brandizzi, Fracture behaviour of nickel-titanium laser welded joints, J. Mater. Eng. Perform. 18 (2009) 569–574, http://dx.doi.org/10.1007/s11665-009-9351-8.
[22] J.P. Oliveira, B. Panton, Z. Zeng, T. Omori, Y. Zhou, R.M. Miranda, F.M. Braz Fernandes, Laser welded superelastic Cu–Al–Mn shape memory alloy wires, Mater. Des. 90 (2016) 122–128, http://dx.doi.org/10.1016/j.matdes.2015.10.125.
[23] J.P. Oliveira, Z. Zeng, T. Omori, N. Zhou, R.M. Miranda, F.M.B. Fernandes, Improvement of damping properties in laser processed superelastic Cu-Al-Mn shape memory alloys, Mater. Des. 98 (2016) 280–284, http://dx.doi.org/10.1016/j.matdes.2016.03.032.
[24] C.A. Biffi, B. Previtali, A. Tuissi, Microstructure and calorimetric behavior of laser welded open cell foams in CuZnAl shape memory alloy, Funct. Mater. Lett. 9 (2016) 1642007, http://dx.doi.org/10.1142/S1793604716420078.
[25] B. Tam, A. Pequegnat, M.I. Khan, Y. Zhou, Resistance microwelding of Ti-55.8 wt pct ni nitinol wires and the effects of pseudoelasticity, Metall. Mater. Trans. A Phys. Metall. Mater. Sci. 43 (2012) 2969–2978, http://dx.doi.org/10.1007/s11661-012-1115-7.
[26] J.P. Oliveira, D. Barbosa, F.M.B. Fernandes, R.M. Miranda, Tungsten inert gas (TIG) welding of Ni-rich NiTi plates: functional behavior, Smart Mater. Struct. 25 (2016) 03LT01, http://dx.doi.org/10.1088/0964-1726/25/3/03LT01.
[27] G. Fox, R. Hahnlen, M.J. Dapino, Fusion welding of nickel-titanium and 304 stainless steel tubes: part II: tungsten inert gas welding, J. Intell. Mater. Syst. Struct. 24 (2013) 962–972, http://dx.doi.org/10.1177/1045389X12461076.
[28] D.S. Grummon, J.A. Shaw, J. Foltz, Fabrication of cellular shape memory alloy materials by reactive eutectic brazing using niobium, Mater. Sci. Eng. A 438–440 (2006) 1113–1118, http://dx.doi.org/10.1016/j.msea.2006.03.113.
[29] X.K. Zhao, J.W. Tang, L. Lan, J.H. Haung, H. Zhang, Y. Wang, Vacuum brazing of NiTi alloy by AgCu eutectic filler, Mater. Sci. Technol. 25 (2009) 1495–1497, http://dx.doi.org/10.1179/174328409X405625.
[30] S. Belyaev, V. Rubanik, N. Resnina, V. Rubanik, I. Lomakin, Functional properties of “Ti 50 Ni 50–Ti 49.3 Ni 50.7” shape memory composite produced by explosion welding, Smart Mater. Struct. 23 (2014) 85029, http://dx.doi.org/10.1088/0964-1726/23/8/085029.
[31] D. Yang, H.C. Jiang, M.J. Zhao, L.J. Rong, Microstructure and mechanical behaviors of electron beam welded NiTi shape memory alloys, Mater. Des. 57 (2014) 21–25, http://dx.doi.org/10.1016/j.matdes.2013.12.039.
[32] J.P. Oliveira, F.M.B. Fernandes, R.M. Miranda, N. Schell, J.L. Ocaña, Residual stress analysis in laser welded NiTi sheets using synchrotron X-ray diffraction, Mater. Des. 100 (2016) 180–187, http://dx.doi.org/10.1016/j.matdes.2016.03.137.
[33] D. Ruhlig, H. Gugel, A. Schulte, W. Theisen, W. Schuhmann, Visualization of local electrochemical activity and local nickel ion release on laser-welded NiTi/steel joints using combined alternating current mode and stripping mode SECM, Analyst 133 (2008) 1700–1706, http://dx.doi.org/10.1039/b804718a.
[34] C.W. Chan, H.C. Man, T.M. Yue, Effect of postweld heat treatment on the microstructure and cyclic deformation behavior of laser-welded NiTi-shape memory wires, Metall. Mater. Trans. A. 43 (2012) 1956–1965, http://dx.doi.org/10.1007/s11661-011-1062-8.
[35] P. Sevilla, F. Martorell, C. Libenson, J.A. Planell, F.J. Gil, Laser welding of NiTi orthodontic archwires for selective force application, J. Mater. Sci. Mater. Med. 19 (2008) 525–529, http://dx.doi.org/10.1007/s10856-007-0164-8.
[36] J.P. Oliveira, F.M. Braz Fernandes, R.M. Miranda, N. Schell, J.L. Ocaña, Effect of laser welding parameters on the austenite and martensite phase fractions of NiTi, Mater. Charact. 119 (2016) 148–151, http://dx.doi.org/10.1016/j.matchar.2016.08.001.
[37] A. Falvo, F.M.M. Furgiuele, C. Maletta, Functional behaviour of a NiTi-welded joint: two-way shape memory effect, Mater. Sci. Eng. A 481–482 (2008) 647–650, http://dx.doi.org/10.1016/j.msea.2006.11.178.
[38] Y.G.G. Song, W.S.S. Li, L. Li, Y.F.F. Zheng, The influence of laser welding parameters on the microstructure and mechanical property of the as-jointed NiTi alloy wires, Mater. Lett. 62 (2008) 2325–2328, http://dx.doi.org/10.1016/j.matlet.2007.11.082.
[39] W.M. Steen, J. Mazumder, Laser Material Processing, Springer London, London, 2010, http://dx.doi.org/10.1007/978-1-84996-062-5.
[40] Z. Sun, J.C. Ion, Review laser welding of dissimilar metal combinations, J. Mater. Sci. 30 (1995) 4025–4214, http://dx.doi.org/10.1007/BF00361499.
[41] Y. Javadi, M.A. Najafabadi, Comparison between contact and immersion ultrasonic method to evaluate welding residual stresses of dissimilar joints, Mater. Des. 47 (2013) 473–482, http://dx.doi.org/10.1016/j.matdes.2012.12.069.
[42] T.A. Mai, A.C. Spowage, Characterisation of dissimilar joints in laser welding of steel–kovar, copper–steel and copper–aluminium, Mater. Sci. Eng. A 374 (2004) 224–233, http://dx.doi.org/10.1016/j.msea.2004.02.025.
[43] Y. Javadi, M. Ashoori, Sub-surface stress measurement of cross welds in a dissimilar welded pressure vessel, Mater. Des. 85 (2015) 82–90, http://dx.doi.org/10.1016/j.matdes.2015.07.012.
[44] W. Ren, F. Lu, R. Yang, X. Liu, Z. Li, S.R. Elmi Hosseini, A comparative study on fiber laser and CO_2 laser welding of Inconel 617, Mater. Des. 76 (2015) 207–214, http://dx.doi.org/10.1016/j.matdes.2015.03.033.
[45] H. Gugel, W. Theisen, Microstructural investigations of laser welded dissimilar nickel-titanium-steel joints, ESOMAT 2009 - 8th Eur. Symp. Martensitic Transform. 5009 (2009) 0–5, http://dx.doi.org/10.1051/esomat/200905009.
[46] H. Gugel, A. Schuermann, W. Theisen, Laser welding of NiTi wires, Mater. Sci. Eng. A 481–482 (2008) 668–671, http://dx.doi.org/10.1016/j.msea.2006.11.179.
[47] J. Vannod, M. Bornert, J.-E. Bidaux, L. Bataillard, A. Karimi, J.-M. Drezet, M. Rappaz, A. Hessler-Wyser, Mechanical and microstructural integrity of nickel–titanium and stainless steel laser joined wires, Acta Mater. 59 (2011) 6538–6546, http://dx.doi.org/10.1016/j.actamat.2011.06.031.
[48] P. Burdet, J. Vannod, A. Hessler-Wyser, M. Rappaz, M. Cantoni, Three-dimensional chemical analysis of laser-welded NiTi–stainless steel wires using a dual-beam FIB, Acta Mater. 61 (2013) 3090–3098, http://dx.doi.org/10.1016/j.actamat.2013.01.069.
[49] R. Hahnlen, G. Fox, M.J. Dapino, Fusion welding of nickel-titanium and 304 stainless steel tubes: part I: laser welding, J. Intell. Mater. Syst. Struct. 24 (2012) 945–961, http://dx.doi.org/10.1177/1045389X12461075.
[50] A. Shojaei Zoeram, S.A.A. Akbari Mousavi, Laser welding of Ti–6Al–4V to nitinol, Mater. Des. 61 (2014) 185–190, http://dx.doi.org/10.1016/j.matdes.2014.04.078.
[51] J.P. Oliveira, B. Panton, Z. Zeng, C.M. Andrei, Y. Zhou, R.M. Miranda, F.M.B. Fernandes, Laser joining of NiTi to Ti6Al4V using a niobium interlayer, Acta Mater. 105 (2016) 9–15, http://dx.doi.org/10.1016/j.actamat.2015.12.021.
[52] X. Chen, A. Hehr, M.J. Dapino, P.M. Anderson, Deformation mechanisms in NiTi-Al composites fabricated by ultrasonic additive manufacturing, Shape Mem. Superelasticity 1 (2015) 294–309, http://dx.doi.org/10.1007/s40830-015-0032-1.
[53] A. Hehr, M.J. Dapino, Interfacial shear strength estimates of NiTi e Al matrix composites fabricated via ultrasonic additive manufacturing, Compos. Part B 77 (2015) 199–208, http://dx.doi.org/10.1016/j.compositesb.2015.03.005.
[54] J.P. Oliveira, J.F. Duarte, P. Inácio, N. Schell, R.M. Miranda, T.G. Santos, Production of Al/NiTi composites by friction stir welding assisted by electrical current, Mater. Des. 113 (2017) 311–318, http://dx.doi.org/10.1016/j.matdes.2016.10.038.
[55] F.A. Stevie, C.B. Vartuli, L.A. Giannuzzi, T.L. Shofner, S.R. Brown, B. Rossie, F. Hillion, R.H. Mills, M. Antonell, R.B. Irwin, B.M. Purcell, Application of focused ion beam lift-out specimen preparation to TEM, SEM, STEM, AES and SIMS analysis, Surf. Interface Anal. 31 (2001) 345–351, http://dx.doi.org/10.1002/sia.1063.
[56] T. Soysal, S. Kou, D. Tat, T. Pasang, Macrosegregation in dissimilar-metal fusion welding, Acta Mater. 110 (2016) 149–160, http://dx.doi.org/10.1016/j.actamat.2016.03.004.
[57] L. Xiao, L. Liu, Y. Zhou, S. Esmaeili, Resistance-spot-welded AZ31 magnesium alloys: part I. Dependence of fusion zone microstructures on second-phase particles, Metall. Mater. Trans. A Phys. Metall. Mater. Sci. 41 (2010) 1511–1522, http://dx.doi.org/10.1007/s11661-010-0197-3.
[58] H. Du, Y. Fu, Deposition and characterization of Ti1 − x(Ni,Cu)x shape memory alloy thin films, Surf. Coat. Technol. 176 (2004) 182–187, http://dx.doi.org/10.1016/S0257-8972(03)00625-X.
[59] J.P. Oliveira, F.M.B. Fernandes, N. Schell, R.M. Miranda, Martensite stabilization during superelastic cycling of laser welded NiTi plates, Mater. Lett. 171 (2016) 273–276, http://dx.doi.org/10.1016/j.matlet.2016.02.107.
[60] P. Sedmák, P. Šittner, J. Pilch, C. Curfs, Instability of cyclic superelastic deformation of NiTi investigated by synchrotron X-ray diffraction, Acta Mater. 94 (2015) 257–270, http://dx.doi.org/10.1016/j.actamat.2015.04.039.
[61] S. Miyazaki, T. Imai, Y. Igo, K. Otsuka, Effect of cyclic deformation on the psedoelasticity characteristics of Ti-Ni alloys, Metall. Trans. A, Phys. Metall. Mater. Sci. 17 (A) (1986) 115–120 http://www.scopus.com/inward/record.url?eid=2-s2.0-0022544716&partnerID=tZOtx3y1.
[62] P. Sedmak, J. Pilch, L. Heller, J. Kopecek, J. Wright, P. Sedlak, M. Frost, P. Sittner, Grain-resolved analysis of localized deformation in nickel-titanium wire under tensile load, Science 353 (2016) 559 (80-.), http://dx.doi.org/10.1126/science.aad6700.